



Cite this: *Energy Adv.*, 2025,  
4, 565

## Design parameter optimization of a membrane reactor for methanol synthesis using a sophisticated CFD model†

Theresa Hauth, \* Konstantin Pielmaier, Vincent Dieterich, Nicolas Wein, Hartmut Spliethoff and Sebastian Fendt

Carbon capture and utilization technologies are considered crucial in reducing carbon dioxide levels in the atmosphere and mitigating climate change. One of the most promising utilization options is the catalytic hydrogenation of the captured carbon dioxide to methanol. However, this reaction requires large energy-consuming recycles due to the limitation of the chemical equilibrium. To shift the chemical equilibrium and increase per-pass conversion, membrane reactors that remove the produced water from the reaction zone can be applied. A sophisticated CFD model of the membrane reactor with a NaA zeolite membrane is developed, to identify key constructive and operating parameters. The model implements the Maxwell–Stefan approach for permeation that considers the complex behavior of pervaporating water–alcohol mixtures through microporous zeolite membranes. In a full-factorial design of experiment, two general categories of parameters (ratio between reaction and permeation, permeation driving force) that influence conversion and yield in membrane reactors are identified that need to be optimized in construction and operation. In the most promising configuration, the application of the membrane reactor results in an increased  $\text{CO}_2$  conversion of 20.6% and a 16.0% enhanced methanol yield compared to an equivalent conventional reactor. With the findings of this study, key parameters for the general optimization of the construction and operation of membrane reactors for industrial applications are identified.

Received 16th January 2025,  
Accepted 20th February 2025

DOI: 10.1039/d5ya00016e

rsc.li/energy-advances

## 1 Introduction

According to the Intergovernmental Panel on Climate Change (IPCC), human emission of greenhouse gases (GHGs) has unequivocally led to global warming.<sup>1</sup> In the last 50 years, the global surface temperature has been increasing faster than in any other comparable period of time over the last 2000 years due to the consumption of fossil fuels for energy production and transportation.<sup>1</sup> As a consequence, the frequency as well as the intensity of heat waves, heavy precipitation events, and droughts have increased, causing substantial damage and irreversible loss in global ecosystems.<sup>1</sup>

To reduce the atmospheric level of carbon dioxide ( $\text{CO}_2$ ) as the main anthropogenic GHG and mitigate global warming, carbon capture and storage (CCS) is considered a crucial technology by permanently sequestering  $\text{CO}_2$  in geological storages

such as aquifers.<sup>1–3</sup> Alternatively, carbon capture and utilization (CCU) is gaining significant attention by recycling  $\text{CO}_2$  and providing non-fossil carbonaceous feedstocks to industry.<sup>3,4</sup> Catalytic hydrogenation of captured  $\text{CO}_2$  to methanol ( $\text{CH}_3\text{OH}$ ) is one of the most promising CCU pathways because of its high revenue stream, partially recovering the costs of capturing  $\text{CO}_2$ , and its technological maturity.<sup>3–5</sup>

With an estimated market size of 43.91 billion U.S. dollars in 2024,  $\text{CH}_3\text{OH}$  is a versatile chemical feedstock as precursor to acetic acid (7% of total  $\text{CH}_3\text{OH}$  demand), formaldehyde (23%), methyl *tert*-butyl ether (MTBE) (11%), and olefins (31%).<sup>6,7</sup> Due to the liquid state of  $\text{CH}_3\text{OH}$  at ambient temperature and the related simple handling, it is also discussed as an alternative fuel (17%) as well as a potential chemical energy storage for fluctuating renewable energy sources.<sup>7,8</sup>

The formation of  $\text{CH}_3\text{OH}$  proceeds predominantly *via*  $\text{CO}_2$  hydrogenation following eqn (1a), even when using carbon monoxide (CO) rich feedstock.<sup>9</sup> Thus, the hydrogenation of CO according to eqn (1b) occurs scarcely. The reverse water–gas shift (RWGS) reaction shown in eqn (1c) denotes the competing conversion of  $\text{CO}_2$  to CO by consumption of hydrogen ( $\text{H}_2$ ). The stoichiometric ratio indicates that a  $\text{H}_2$  to  $\text{CO}_2$  feed gas ratio of

Chair of Energy Systems, Technical University of Munich, Boltzmannstr.15, 85748 Garching, Germany. E-mail: [theresa.hauth@tum.de](mailto:theresa.hauth@tum.de), [sebastian.fendt@tum.de](mailto:sebastian.fendt@tum.de); Tel: +49 89 289 16344

† Electronic supplementary information (ESI) available. See DOI: <https://doi.org/10.1039/d5ya00016e>



3 to 1 is optimal for the process.<sup>9</sup> A higher CO<sub>2</sub> concentration inhibits CH<sub>3</sub>OH synthesis due to a rise in water (H<sub>2</sub>O) formation following the RWGS reaction.<sup>9</sup> Due to the exothermicity and the volume decrease of the hydrogenation reaction, CH<sub>3</sub>OH synthesis is favored by low temperatures and elevated pressures.<sup>9</sup> The endothermic RWGS reaction expedites the formation of the undesired by-products CO and H<sub>2</sub>O, reducing CH<sub>3</sub>OH selectivity.<sup>4</sup>



Historically, industrial-scale CH<sub>3</sub>OH synthesis was performed at high pressures (250 bar to 350 bar) and temperatures (320 °C to 450 °C).<sup>9</sup> Due to catalyst advances in the 1960s, today, lower operational pressures of 50 bar to 100 bar and temperatures of 200 °C to 300 °C are sufficient for CH<sub>3</sub>OH production.<sup>9</sup>

Commercially, heterogenic copper/zinc-oxide (Cu/ZnO) catalysts on supports such as alumina (Al<sub>2</sub>O<sub>3</sub>) designed for the hydrogenation of synthesis gas to CH<sub>3</sub>OH are used to convert CO<sub>2</sub> feedstock.<sup>9,10</sup> Specialized catalysts using main group metal oxides (e.g. In<sub>2</sub>O<sub>3</sub>), intermetallic composites (e.g. Ni-Ga), or nanostructured supports (e.g. metal oxide frameworks (MOFs)) are potential candidates for the promotion of activity, selectivity and stability in CO<sub>2</sub> hydrogenation to CH<sub>3</sub>OH.<sup>10</sup>

Two main challenges have to be addressed during reactor design for CH<sub>3</sub>OH synthesis. First, the formed heat of the reaction needs to be removed economically.<sup>9,11–13</sup> Industry has come up with a variety of possible solutions, including the generation of medium-pressure steam in a steam-raising fixed bed reactor (e.g. Lurgi tubular reactor) or preheating the feed with the generated reaction heat (e.g. ICI tube-cooled converter). Affiliating, several companies have combined both solutions to reduce the overall heat demand as well as the operating costs by effective energy integration in two coupled reactors (e.g. Johnson Matthey Combi Loop, Mitsubishi Super-converter, Lurgi MegaMethanol).<sup>9,11–13</sup> A summary of operating reactor concepts is provided in several reviews.<sup>9,11–14</sup>

Second, due to the chemical equilibrium of the hydrogenation reactions, single-pass CH<sub>3</sub>OH yield is limited.<sup>12</sup> Compared to the conventional CH<sub>3</sub>OH synthesis from synthesis gas, the use of CO<sub>2</sub> as feedstock decreases the single-pass conversion even more, resulting in an even higher recycle duty and consequently higher operating costs.<sup>15</sup> In literature, several concepts have been experimentally tested or simulated to shift the chemical equilibrium and decrease the required compression duty by removing reaction products. Bos *et al.* achieved a carbon yield above 99.5% using a small laboratory scale reactor with liquid-out-gas-in concept (LOGIC). By lowering the temperature above the catalyst bed, H<sub>2</sub>O and CH<sub>3</sub>OH are condensed and unreacted gases are recycled back into the catalyst bed *in situ*.<sup>16,17</sup> A different approach is taken by Kuczynski *et al.*, who were able to achieve full conversion in one pass by incorporating CH<sub>3</sub>OH adsorbing silica-alumina particles into the

catalytic fixed bed. These so-called sorption-enhanced reactors are frequently discussed in literature and show potential for enhanced carbon conversion. In a simulative study, Arora *et al.* present a H<sub>2</sub>O adsorbing NaX zeolite sorption-enhanced reactor that increases CH<sub>3</sub>OH yield compared to a traditional reactor (TR) by 8.17%.<sup>18,19</sup> Another approach to shift the chemical equilibrium is introducing a permselective membrane into the reaction zone that removes one or both reaction products. Thus, improving CO<sub>2</sub> conversion, CH<sub>3</sub>OH selectivity, and CH<sub>3</sub>OH yield with less recycling effort than TRs; potentially decreasing the reactor's size, energy demand, and ultimately costs.<sup>20,21</sup> Struis *et al.* first provided proof of the benefit of using membrane reactors (MRs) for CH<sub>3</sub>OH synthesis in 1995.<sup>22</sup> A perfluorinated cation exchange Nafion membrane separates the reaction products, resulting in an increase of CH<sub>3</sub>OH yield by 2.5% compared to a TR.<sup>22</sup> However, as Nafion is not stable at temperatures above 205 °C, different membrane materials have been investigated.<sup>22,23</sup> In 2003, Gallucci *et al.* published their work on MRs for CH<sub>3</sub>OH synthesis implementing an A-type zeolite membrane that separates H<sub>2</sub>O and CH<sub>3</sub>OH. With an increase of CO<sub>2</sub> conversion of 6.3% compared to a TR, Gallucci *et al.* state that the same conversion rates can be achieved at lower operating conditions in a MR. However, due to the necessity of pore condensation for permeation, the operating parameters should not surpass the critical parameters of CH<sub>3</sub>OH.<sup>24</sup> Tran *et al.* applied a MR with a NaA zeolite membrane manufactured by the Fraunhofer Institute for Ceramic Technologies and Systems (IKTS) at low pressures between 3 and 7 bar reporting an increased CH<sub>3</sub>OH space time yield compared to a TR.<sup>25</sup> Li *et al.* also adopted a NaA zeolite membrane in a small-scale reactor and obtained a CO<sub>2</sub> conversion of up to 61.4% with an increase in CH<sub>3</sub>OH yield of up to 38.9%. Demonstrating a 95% *in situ* removal of H<sub>2</sub>O, Li *et al.* state to have achieved the highest space time yield published for CH<sub>3</sub>OH synthesis from CO<sub>2</sub> hydrogenation in literature.<sup>26</sup>

Several researchers have investigated additional materials for membranes in CH<sub>3</sub>OH synthesis, revealing the great potential to increase per-pass conversion.<sup>21,27,28</sup> However, there is a lack of research concentrating on the actual realization of MRs for CH<sub>3</sub>OH synthesis and the in-depth optimal reactor design as well as operating principle.

For simplified reactor prototyping, computational fluid dynamics (CFD) is a fast and cost-effective approach that allows the analysis of the influence and interactions of constructive and operating parameters. In literature, several mathematical models regarding CH<sub>3</sub>OH synthesis in MRs exist, investigating the behavior of the reaction with various membranes and operating conditions. Samimi *et al.* analyse the potential of MRs in the CAMERE process, that combines CH<sub>3</sub>OH synthesis with a prior RWGS reactor. By implementing an hydroxy sodalite (H-SOD) membrane in the two-dimensional simulation, the CH<sub>3</sub>OH production rate was increased by 20.8%.<sup>29</sup> Thermodynamic analysis of a MR for CH<sub>3</sub>OH synthesis from Barbieri *et al.* shows significant increase in conversion, selectivity and yield.<sup>30</sup> Ountaksinkul *et al.* compare different MR constructions with two-dimensional CFD models revealing the



potential of planar micro-structured MRs for  $\text{CH}_3\text{OH}$  synthesis.<sup>31</sup> Hamedi *et al.* present a one-dimensional model of a H-SOD MR for  $\text{CH}_3\text{OH}$  synthesis that incorporates back diffusion of permeated species. An increase in  $\text{CO}_2$  conversion is shown when implementing a non-adiabatic over an adiabatic MR. However, both MRs result in an improved conversion compared to a TR.<sup>32</sup> A general approach for the design of MRs to enhance thermodynamically-limited reactions is provided by Huang *et al.* For reactor optimization, the dimensionless parameter DaPe (Damköhler Pécelt) is introduced describing the compatibility of the reaction kinetics and the permeation flux. Applied to the dry reforming of methane and the RWGS reaction, reactor geometry and operating principles are improved, resulting in an increased conversion.<sup>33</sup>

All aforementioned models use simple descriptions of product permeation implementing empirical equations for  $\text{H}_2\text{O}$  permeance with permeability coefficients and partial pressure differences. Thereby, the interactions between competing permeating species are overlooked, resulting in an inaccurate description of permeation and, eventually, an improper analysis of MRs for  $\text{CH}_3\text{OH}$  synthesis. In this work, a sophisticated novel approach for the description of reactant and product permeation in a MR for  $\text{CH}_3\text{OH}$  synthesis is adopted based on the permeation model of Maxwell–Stefan (M–S) that considers the findings of Krishna and van Baten concerning the distinct characteristics of pervaporating water–alcohol mixtures in zeolite membranes.<sup>34–36</sup> The approach incorporates the interactions between different permeating species by considering all individual species in the mixture, the forces applied to them, and the resulting induced motions.<sup>34,35</sup> Accounting for the interactions between species is particularly crucial in water–alcohol mixtures, where coupling effects significantly impact permeation, resulting in the inapplicability of unary diffusion coefficients, the uncoupled M–S formulation, and Vignes interpolation.<sup>37</sup> With the more general M–S approach, the model can be easily adapted to different applications, as the model, as well as the coefficients, are independent of the reference frame.<sup>34,36</sup> Additionally, as permeation is a function of temperature, a vant Hoff-type temperature dependence is incorporated for the adsorption model, and an Arrhenius-type temperature dependence is adopted for the diffusion model. Hence, a more comprehensive depiction of multicomponent diffusion through the membrane is applied, resulting in a more accurate analysis of MRs for  $\text{CH}_3\text{OH}$  synthesis.<sup>36</sup>

Using the aforementioned novel approach, the objective of this work is to:

- Implement the novel more detailed permeation model based on the M–S approach in a comprehensive CFD model.
- Improve the understanding of the key parameters that affect  $\text{CO}_2$  conversion and  $\text{CH}_3\text{OH}$  yield in the examined MR.
- Reveal an optimal construction and operating guide for improved  $\text{CH}_3\text{OH}$  synthesis in a MR with a NaA-gated water-conducting membrane.
- Create a systematic approach for virtual prototyping of MRs that can be applied for optimization of various applications.

## 2 Modelling

The simulated membrane reactor (MR) employs a commercial copper–zinc–oxide–alumina (CZA) catalyst and the microporous NaA zeolite membrane developed by Li *et al.*<sup>26</sup> The computational fluid dynamics application Ansys Fluent 2022 R1 is used to create a three-dimensional simulation of the MR. Reaction and permeation are integrated within two user-defined-functions (UDFs).

### 2.1 Geometry and mesh

The MR is designed as a tube-in-tube reactor running in counter-current with an inner membrane and an outer wall as shown in Fig. 1. As thermal boundary conditions, the inside and outside of the membrane are thermally coupled and the outer wall has a constant temperature corresponding to the operating temperature. The synthesis gas feed flows over the catalyst bed between the membrane and the outside wall, whereas the purge gas sweep flows inside the membrane in the opposite direction to maximize the partial pressure difference along the reactor, enhancing permeation. Thus, the inlets as well as the outlets of the synthesis gas and purge gas streams are situated on opposite ends of the reactor. The computer-aided-design (CAD) program SpaceClaim is used to create a

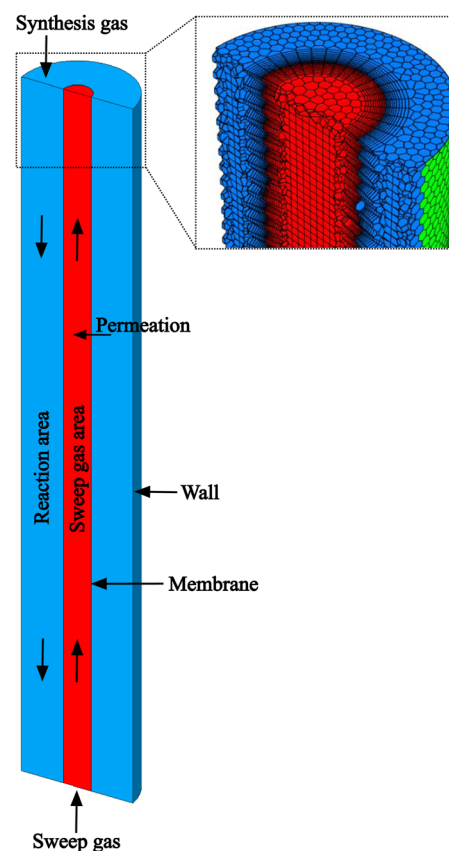


Fig. 1 Cross-section of the simulated MR with the reaction area on the outside of the membrane and the sweep gas area on the inside. Additionally the magnified mesh is indicated with the more detailed boundary layer around the membrane.



Table 1 Geometric parameters of the simulated MR

Parameter	Symbol	Value	Unit
Membrane diameter	$d_m$	10	mm
Membrane thickness	$t_m$	1.5	mm
Wall diameter	$d_w$	40	mm
Wall thickness	$t_w$	6	mm
Length	$l$	250	mm

three-dimensional geometry model of the tubular MR, whose geometric parameters are summarized in Table 1.

The required mathematical discretization is generated based on the spatial geometry model in the meshing mode of Fluent. To ensure sufficient accuracy of the mesh around the membrane, boundary layers are grown into the fluids on either side of the membrane. The poly-hexcore mesh with a minimal and maximal cell size of 0.004 mm and 1.024 mm has an orthogonal quality of 41 across 284 936 cells. A mesh independence study attached in A1 is conducted affirming sufficient grid refinement.<sup>†</sup>

## 2.2 Reaction

Four different volumetric reaction rate UDFs are implemented in Fluent based on the kinetic models by Graaf *et al.*, Vanden Bussche and Froment, Mignard and Pritchard, and Nestler *et al.* to describe CH<sub>3</sub>OH synthesis.<sup>38–42</sup> The kinetic models are validated using the empirical results published by Gallucci *et al.* CO<sub>2</sub> conversion ( $x_{CO_2}$ ) and CH<sub>3</sub>OH selectivity ( $S_{CH_3OH}$ ) are calculated according to eqn (2) and (3). The dimensions of the simulated reactor derived from the experimental setup of Gallucci *et al.*, the corresponding mesh independence study as well as the validation results are attached in A2.1.<sup>24</sup> †

$$x_{CO_2} = \frac{\dot{N}_{CO_2,in} - \dot{N}_{CO_2,out}}{\dot{N}_{CO_2,in}} \times 100 \quad (2)$$

$$S_{CH_3OH} = \frac{\dot{N}_{CH_3OH,out}}{\dot{N}_{CO_2,in} - \dot{N}_{CO_2,out}} \times 100 \quad (3)$$

In this simulative study an inlet feed temperature of 250 °C is employed to account for the highest kinetically achievable CO<sub>2</sub> conversion.<sup>30</sup> Analyzing the kinetic regressions, the related models developed by Vanden Bussche and Froment and Mignard and Pritchard show the most accurate reproduction of the experimental data at the specific operation temperature. Based on the knowledge that CO<sub>2</sub> is the main source of CH<sub>3</sub>OH, both kinetic models neglect the CH<sub>3</sub>OH synthesis route *via* CO and only regard CO<sub>2</sub> hydrogenation and RWGS reaction.<sup>41</sup> Mignard and Pritchard adjust the activation energies of both reactions from the kinetic model of Vanden Bussche and Froment to improve the sensitivity of the model at lower temperatures.<sup>41</sup> Moreover, since the adjustment extends the range of applicability of the model by Vanden Bussche and Froment in terms of pressure from 51 bar to 75 bar, the model by Mignard and Pritchard is selected for the description of the CH<sub>3</sub>OH synthesis reaction mechanism.<sup>40,41</sup> The corresponding reaction rates are specified in eqn (4) and (5).<sup>41</sup> The necessary

Table 2 Parameters of the kinetic model by Vanden Bussche and Froment modified by Mignard and Pritchard based on the chemical equilibria by Graaf *et al.*

Parameter	Unit	Equation	Source
$k_1$	mol s <sup>-1</sup> kg bar <sup>2</sup>	$1.07 \exp\left(\frac{40\ 000}{RT}\right)$	41
$k_2$	mol s <sup>-1</sup> kg bar	$1.22 \times 10^{10} \exp\left(\frac{-98\ 084}{RT}\right)$	41
$K_{H_2O}$	1 bar <sup>-1</sup>	$6.62 \times 10^{-11} \exp\left(\frac{124\ 119}{RT}\right)$	40
$K_{H_2}^{1/2}$	1 bar <sup>-1/2</sup>	$0.499 \exp\left(\frac{17\ 197}{RT}\right)$	40
$K_{H_2O,H_2}$	—	3453.38	40
$K_{eq,1}$	1 bar <sup>-2</sup>	$10^{\frac{3066}{T} - 10.592}$	43
$K_{eq,2}$	—	$10^{\frac{-2073}{T} + 2.029}$	43

constants are listed in Table 2 including the chemical equilibrium constants based on Graaf *et al.*<sup>41,43</sup> To assess the accurate integration of the kinetic model, the reaction UDF is additionally validated in A2.2 with simulative data obtained by Bussche and Froment.<sup>40</sup> †

$$r_{CO_2} = \frac{k_1 p_{CO_2} p_{H_2} \left(1 - \frac{p_{H_2O} p_{CH_3OH}}{K_{eq,1} p_{H_2}^3 p_{CO_2}}\right)}{\left(1 + \frac{K_{H_2O,H_2} p_{H_2O}}{p_{H_2}} + (K_{H_2} p_{H_2})^{1/2} + K_{H_2O} p_{H_2O}\right)^3} \quad (4)$$

$$r_{RWGS} = \frac{k_2 p_{CO_2} \left(1 - \frac{p_{H_2O} p_{CO}}{K_{eq,2} p_{H_2} p_{CO_2}}\right)}{\left(1 + \frac{K_{H_2O,H_2} p_{H_2O}}{p_{H_2}} + (K_{H_2} p_{H_2})^{1/2} + K_{H_2O} p_{H_2O}\right)^3} \quad (5)$$

## 2.3 Permeation

The employed membrane consists of sodium ion (Na<sup>+</sup>)-gated water-conducting nanochannels with a diameter of 4.2 Å which impede the permeation of gas molecules and strain H<sub>2</sub>O from the reaction zone.<sup>26</sup> Due to the high H<sub>2</sub>O permselectivities against CO and CO<sub>2</sub> of the hydrophilic membrane developed by Li *et al.*, only the permeation of H<sub>2</sub>O, CH<sub>3</sub>OH, and H<sub>2</sub> is considered.<sup>26</sup> The process of permeation across the microporous membrane is modeled with a novel method for CFD simulation, which properly considers the interactions between water and alcohol species. According to Krishna *et al.*, mixture permeation across zeolite membranes can be expressed most properly by the multicomponent Langmuir approach for adsorption and the Maxwell-Stefan (M-S) approach for diffusion.<sup>36</sup> Whereas the Langmuir approach is based on the Langmuir adsorption parameters ( $b_i$ ), the M-S approach uses the species M-S diffusivities ( $D_{ij}$ ), which reflect the interactions between the species *i* and the zeolite membrane, as well as the exchange M-S diffusivities ( $D_{ij}$ ), which reflect the interaction between species *i* and *j*.<sup>37</sup> A temperature dependence is incorporated with a van't Hoff type temperature dependence of adsorption for the Langmuir adsorption parameters shown in eqn (6) as well as an Arrhenius



Table 3 Values used in the permeation UDF with literature sources

Symbol	Value	Unit	Source
$\rho_m$	1900	$\text{kg m}^{-3}$	44
$b_{\text{o},\text{H}_2\text{O}}$	$1.64 \times 10^{-12}$	$1 \text{ Pa}^{-1}$	Fitted values
$b_{\text{o},\text{CH}_3\text{OH}}$	$5.64 \times 10^{-15}$	$1 \text{ Pa}^{-1}$	Fitted values
$b_{\text{o},\text{H}_2}$	$3.22 \times 10^{-9}$	$1 \text{ Pa}^{-1}$	Fitted values
$\Delta H_{\text{ads},\text{H}_2\text{O}}$	-40	$\text{kJ mol}^{-1}$	45
$\Delta H_{\text{ads},\text{CH}_3\text{OH}}$	-65	$\text{kJ mol}^{-1}$	46
$\Delta H_{\text{ads},\text{H}_2}$	-5.9	$\text{kJ mol}^{-1}$	47
$q_{\text{sat},\text{H}_2\text{O}}$	15	$\text{mol kg}^{-1}$	46
$q_{\text{sat},\text{CH}_3\text{OH}}$	6.2	$\text{mol kg}^{-1}$	46
$q_{\text{sat},\text{H}_2}$	1	$\text{mol kg}^{-1}$	48
$D_{\text{o},\text{H}_2\text{O}}$	$7.08 \times 10^{-4}$	$\text{m}^2 \text{s}^{-1}$	37,49
$D_{\text{o},\text{CH}_3\text{OH}}$	$1.03 \times 10^{-7}$	$\text{m}^2 \text{s}^{-1}$	37,49
$D_{\text{o},\text{H}_2}$	$1.7 \times 10^{-8}$	$\text{m}^2 \text{s}^{-1}$	47
$D_{\text{H}_2\text{O},\text{CH}_3\text{OH}}$	$3 \times 10^{-9}$	$\text{m}^2 \text{s}^{-1}$	37
$E_{\text{A},\text{H}_2\text{O}}$	36	$\text{kJ mol}^{-1}$	49
$E_{\text{A},\text{CH}_3\text{OH}}$	17	$\text{kJ mol}^{-1}$	49
$E_{\text{A},\text{H}_2}$	1.9	$\text{kJ mol}^{-1}$	47

type temperature dependence of diffusion for the Maxwell–Stefan diffusivities shown in eqn (7). Table 3 comprises all parameters used in the permeation UDF with their respective sources.<sup>36</sup>

$$b_i = b_{\text{o},i} e^{-\frac{\Delta H_{\text{ads},i}}{RT}} \quad (6)$$

$$D_i = D_{\text{o},i} e^{-\frac{\Delta E_{\text{A},i}}{RT}} \quad (7)$$

As Langmuir adsorption equilibrium constants are missing in literature, the experimental data of Li *et al.* is used to fit the parameters.<sup>26</sup> By contrast, the species M–S diffusivities are readily available in literature. Moreover, based on Vignes interpolation, Krishna and Wesselingh propose eqn (8) to predict the exchange M–S diffusivities by interpolating the species' M–S diffusivities.<sup>50</sup>

$$D_{ij} = D_i^{\frac{\theta_i}{\theta_i + \theta_j}} D_j^{\frac{\theta_j}{\theta_i + \theta_j}} \quad (8)$$

Furthermore, Krishna and Wesselingh state for ideal gas mixtures, the M–S exchange coefficients in a ternary mixture are identical to those in the corresponding binary pairs.<sup>51</sup> Additionally, the Onsager reciprocal relation displayed in eqn (9) holds, with the net effect that the faster-moving species decelerates and the slower-moving species accelerates.<sup>36</sup>

$$D_{ij} = D_{ji} \quad (9)$$

High exchange M–S diffusivities indicate small correlations between the permeating species.<sup>37</sup> For zeolite frameworks like LTA, which allow only one molecule at a time to jump from one cage to the neighboring one, correlations can be negligible leading to a set of uncoupled M–S equations.<sup>37</sup> However, Krishna and van Baten identify several pitfalls for M–S modeling of water–alcohol mixture permeation across pervaporation membranes resulting from two types of diffusional coupling effects.<sup>37,52</sup> The first type are correlation effects, when the less mobile species slows down its more mobile partner by not vacating an adsorption site quickly enough for its more mobile partner to occupy that position.<sup>52</sup> The second type is molecular

clustering due to hydrogen bonding, which can cause the mutual slowing down of the partner molecules.<sup>52</sup> The coupling effects have the following consequences for modeling permeation of water–alcohol mixtures:

- The species M–S diffusivities are lower than for their respective pure components. Thus, the species M–S diffusivities can not be obtained from unary permeation data.<sup>37,52</sup>
- Due to increased correlation, the Vignes interpolation formula is inappropriate for the prediction of the exchange M–S diffusivities. It is not hydrogen bonding, *per se*, that contributes to the deviation from the Vignes formula, rather, it is the difference in the degrees of hydrogen bonding between constituent molecular pairs.<sup>37</sup>
- Employing the uncoupled M–S equations is not justified.<sup>37</sup>

Specifically for the CFD model of the present work, this means that the species M–S diffusivities published by Krishna and van Baten, who report the values for water–alcohol mixtures in LTA zeolites for a temperature of 350 K, are incorporated into the permeation UDF.<sup>37</sup> Furthermore, since, the Wesselingh interpolation formula is based on the Vignes interpolation formula, it is not used to calculate the exchange M–S diffusivity between  $\text{H}_2\text{O}$  and  $\text{CH}_3\text{OH}$ . Moreover, the coupled M–S eqn (10)–(14) are applied in the permeation UDF. Therefore, in contrast to other CFD models, by employing the coupled M–S equations, the present work does not disregard the interaction between the different species in a permeating gas mixture. Rather, in the present study, the coupled M–S method is employed for a proper description of multicomponent permeation of water–alcohol mixtures across microporous zeolite membranes.<sup>34,36,37</sup>

$$-\rho_m \frac{\theta_i}{RT} \frac{\partial \mu_i}{\partial z} = \sum_{\substack{j=1 \\ j \neq i}}^n \frac{q_j J_i - q_i J_j}{q_{i,\text{sat}} q_{j,\text{sat}} D_{ij}} + \frac{J_i}{q_{i,\text{sat}} D_i} \quad (10)$$

$$\Gamma_{ij} = \frac{\theta_i}{p_i} \frac{\partial p_i}{\partial \theta_j} = \delta_{ij} + \frac{\theta_i}{\theta_v} \quad (11)$$

$$B_{ii} = \frac{1}{D_i} + \sum_{\substack{j=1 \\ j \neq i}}^n \frac{\theta_i}{D_{ij}} \quad (12)$$

$$B_{ij} = -\frac{\theta_i}{D_{ij}} \quad (13)$$

$$(J) = -\rho_m [q_{\text{sat}}][B]^{-1} [\Gamma] \frac{\partial \theta}{\partial z} \quad (14)$$

The surface coverage ( $\theta$ ) also known as the fractional loading describes the fraction of occupied adsorption sites, as shown in eqn (15), with the molar loading ( $q$ ) and the saturation loading ( $q_{\text{sat}}$ ). Correspondingly, the fraction of empty sites called fractional vacancy ( $\theta_v$ ) is calculated by eqn (16).

$$\theta_i = \frac{q_i}{q_{\text{sat},i}} = \frac{b_i p_i}{1 + \sum_{j=1}^n b_j p_j} \quad (15)$$



Table 4 Results of the gas mixture separation experiments by Li *et al.*<sup>26</sup>

$p, T$ [bar], [°C]	H <sub>2</sub> O permeance [10 <sup>-7</sup> mol m <sup>-2</sup> s Pa]	H <sub>2</sub> O selectivity vs. CH <sub>3</sub> OH [-]	H <sub>2</sub> O flux [kg m <sup>-2</sup> h]
21, 200	1.62–2.03	>49	>138
21, 250	1.56–1.85	>41	0.46–0.56
38, 250	1.40–1.85	>52	0.44–0.68
			0.45–1.11

Table 5 Simulation results of the permeation validation

$p, T$ [bar], [°C]	H <sub>2</sub> O permeance [10 <sup>-7</sup> mol m <sup>-2</sup> s Pa]	H <sub>2</sub> O selectivity vs. CH <sub>3</sub> OH [-]	H <sub>2</sub> O flux [kg m <sup>-2</sup> h]
21, 200	2.07	53.7	0.50
21, 250	1.69	142	0.43
38, 250	1.42	117	0.60

$$\theta_v = 1 - \sum_{i=1}^n \theta_i = \frac{1}{1 + \sum_{j=1}^n b_j p_j} \quad (16)$$

From an implementation perspective, the permeation UDF introduces source terms for the conservation of mass and energy in the cells adjacent to the membrane. The gas mixture separation experiments conducted by Li *et al.* are recreated in simulation to validate the permeation UDF. The experimental results by Li *et al.* are shown in Table 4 and the results of the permeation validation simulated with the permeation UDF are shown in Table 5. Except for a slight overshoot in H<sub>2</sub>O permeance of 1.97% at 21 bar and 200 °C and a slight undershoot of H<sub>2</sub>O flux of 2.27% at 21 bar and 250 °C the simulative results agree with the empirical data by Li *et al.* The mesh independence study of the geometry based on Li *et al.* is attached in A3.<sup>26</sup>†

#### 2.4 Base case scenario

Besides the description of the reaction as well as the permeation in the applied model, base case operating parameters need to be specified. Therefore the following three parameters are adopted in this study:

The gas hourly space velocity (GHSV) is calculated according to eqn (17), with the standard feed volume flow ( $\dot{V}_{\text{feed},N}$ ) and the volume of the reaction zone ( $V_r$ ). The a sweep-to-feed (S/F) ratio is defined by the molar flows of the sweep ( $\dot{N}_{\text{in,sweep}}$ ) and the feed ( $\dot{N}_{\text{in,feed}}$ ) following eqn (18). Lastly, the ratio of membrane surface to reaction volume ( $O_M/V_r$ ) is based on eqn (19) comprising the membrane diameter ( $d_m$ ), the wall diameter ( $d_w$ ) and the length of the reactor ( $l$ ).

$$\text{GHSV} = \frac{\dot{V}_{\text{feed},N}}{V_r} \quad (17)$$

$$\text{S/F} = \frac{\dot{N}_{\text{in,sweep}}}{\dot{N}_{\text{in,feed}}} \quad (18)$$

$$O_M/V_r = \frac{\pi \cdot d_m \cdot l}{\frac{\pi}{4} \cdot l(d_w^2 - d_m^2)} = \frac{4 \cdot d_m}{d_w^2 - d_m^2} \quad (19)$$

If not otherwise specified, the performance of the MR is analysed in a defined base case scenario with a GHSV of 5000 h<sup>-1</sup> resembling a  $\dot{V}_{\text{feed},N}$  of 24.54 L min<sup>-1</sup> with a stoichiometric H<sub>2</sub>:CO<sub>2</sub> ratio of 3:1, a S/F-ratio of 1, no pressure difference between the reaction and sweep zones, and a  $O_M/V_r$ -ratio of 26.67 m<sup>-1</sup>.

## 3 Results and discussion

### 3.1 Operating conditions

First, the correlation between the operating conditions and the output parameters CO<sub>2</sub> conversion (Fig. 2), CH<sub>3</sub>OH selectivity (Fig. 3), and CH<sub>3</sub>OH yield (Fig. 4) of the membrane reactor (MR) is investigated in a commonly employed pressure range of 20–100 bar and temperature range of 200–300 °C. The distinguished

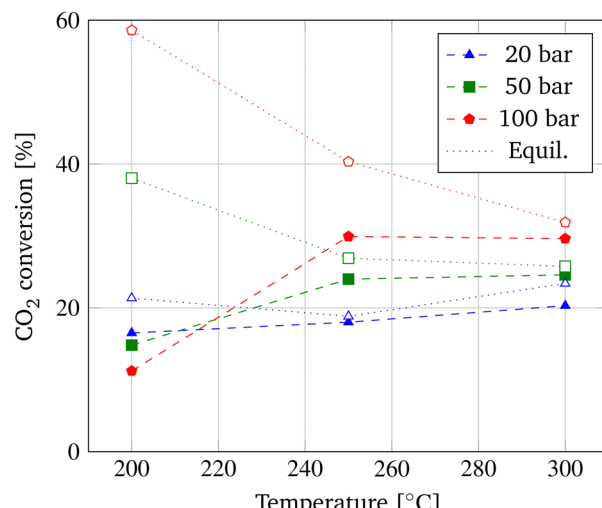


Fig. 2 Pressure and temperature dependency of CO<sub>2</sub> conversion of the MR.

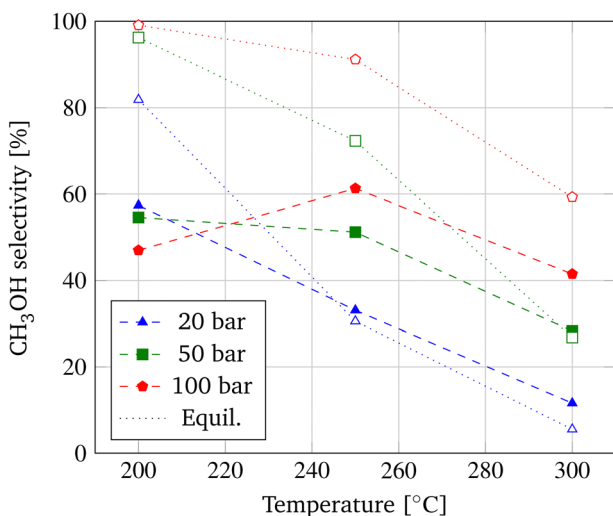


Fig. 3 Pressure and temperature dependency of CH<sub>3</sub>OH selectivity of the MR.



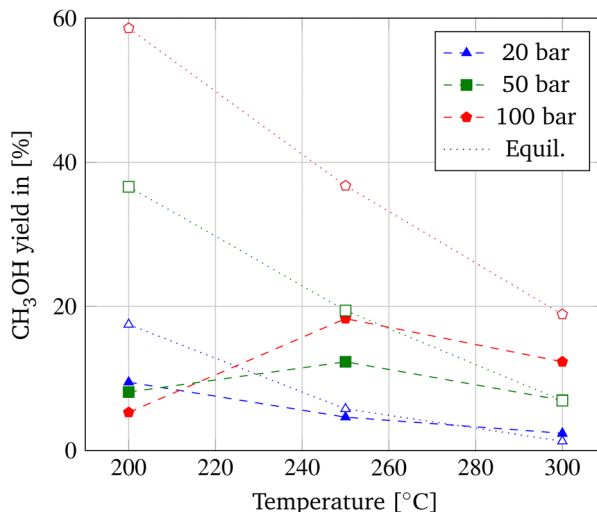


Fig. 4 Pressure and temperature dependency of  $\text{CH}_3\text{OH}$  yield of the MR (dashed lines) and equilibrium  $\text{CH}_3\text{OH}$  yields from ref. 9 (dotted lines).

performance trends of the MR due to equilibrium and kinetic considerations are applicable to methanol synthesis in general. A distinct differentiation between the behavior of a MR and TR is employed subsequently.

According to the principle of Le Châtelier,  $\text{CO}_2$  conversion decreases with temperature due to the exothermic nature of the hydrogenation reaction and increases with pressure as a consequence of the volume-reducing reaction. In Fig. 2, the temperature dependence of the  $\text{CO}_2$  conversion in the MR is displayed alongside the achievable equilibrium  $\text{CO}_2$  conversion derived from Dieterich *et al.*<sup>9</sup> In contrast to the temperature dependency of the chemical equilibrium,  $\text{CO}_2$  conversion in the MR increases with temperature due to the acceleration of the reaction kinetics. Only at a pressure of 100 bar a slight decrease in  $\text{CO}_2$  conversion is apparent from 250 °C to 300 °C. According to Barbieri *et al.*, the resulting maximum in  $\text{CO}_2$  conversion at 250 °C is due to the promotion of  $\text{CO}_2$  activation.<sup>30</sup> At lower pressures, no such optimum at 250 °C is obtained, which could be explained by the less distinctive enhancement of the shift of the equilibrium of the hydrogenation reaction due to pressure and, hence, a different correlation between the competing RWGS and hydrogenation reaction.

This explanation is supported by the behavior of the  $\text{CH}_3\text{OH}$  selectivity shown in Fig. 3, depicting a maximum selectivity to  $\text{CH}_3\text{OH}$  at a temperature of 250 °C and a pressure of 100 bar and a decrease of the selectivity at higher temperatures. This implies that at a temperature of 250 °C, more  $\text{CO}_2$  is converted to  $\text{CH}_3\text{OH}$  in contrast to the formation of undesired  $\text{CO}$  and  $\text{H}_2\text{O}$  due to the RWGS reaction. Due to the smaller significance of the pressure shift of the equilibrium at lower pressures as explained above,  $\text{CH}_3\text{OH}$  selectivity decreases with temperature at pressures of 20 bar and 50 bar following the equilibrium selectivities adopted from Dietreich *et al.*<sup>9</sup>

Eqn (20) depicts the interrelation of  $\text{CH}_3\text{OH}$  yield with  $\text{CO}_2$  conversion and  $\text{CH}_3\text{OH}$  selectivity and explains the comparable behavior of  $\text{CH}_3\text{OH}$  yield with temperature as depicted in Fig. 4.

When referring to the principle of Le Châtelier,  $\text{CO}_2$  conversion should increase with pressure as depicted in Fig. 2 for temperatures above 200 °C and is the same for  $\text{CH}_3\text{OH}$  selectivity and yield. However, at a temperature of 200 °C, the relation is reversed for all three parameters, as also previously reported in experimental data by Gallucci *et al.*<sup>24</sup>

$$y_{\text{CH}_3\text{OH}} = \frac{x_{\text{CO}_2} \cdot S_{\text{CH}_3\text{OH}}}{100\%} \quad (20)$$

This transition of the pressure dependency could be induced by a smaller temperature dependency of the RWGS reaction compared to the hydrogenation reactions. Hence, the water formation due to the RWGS reaction is less imposed at lower temperatures resulting in a higher share of water at low temperatures and high pressures. This explanation could also be the reason why when looking at the  $\text{CH}_3\text{OH}$  yield depicted in Fig. 4 and comparing the achievable equilibrium yield obtainable by  $\text{CO}_2$  hydrogenation included from Dieterich *et al.*, the equilibrium is deviating most at a temperature of 200 °C and higher pressures.<sup>9</sup> The findings correspond to published literature and result in the adoption of a pressure of 100 bar and a temperature of 250 °C in this optimization study of the MR.<sup>26,30</sup>

### 3.2 Permeation characteristics

The performance of the membrane is investigated in a pressure range of 20–100 bar and a temperature range of 200–300 °C. For evaluation, the species removal  $R_i$  is calculated following eqn (21). In Fig. 5, the species removal for the permeating species  $\text{H}_2\text{O}$ ,  $\text{CH}_3\text{OH}$ , and  $\text{H}_2$  are depicted as a function of pressure and temperature.

$$R_i = \frac{\dot{N}_{i,\text{sweep,out}}}{\dot{N}_{i,\text{sweep,out}} + \dot{N}_{i,\text{syngas,out}}} \quad (21)$$

In accordance to the trends observed by Li *et al.*, the species removal increases with increasing pressure.<sup>26</sup> This is due to the

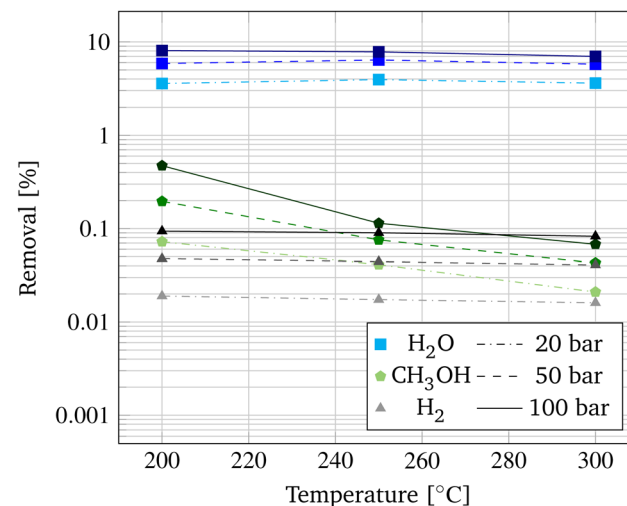


Fig. 5 Species removal by the membrane as a function of pressure and temperature.

enhanced partial pressure difference causing a higher driving force for permeation. Due to the high polarity of the zeolite channels in the membrane, the desired  $\text{H}_2\text{O}$  removal is significantly higher compared to the  $\text{CH}_3\text{OH}$  and  $\text{H}_2$  removal. The in-depth mechanism of the permeation through the  $\text{Na}^+$ -gated zeolite membrane is disclosed by Li *et al.*<sup>26</sup>

In contrast to the pressure dependency on the species removal, an increased temperature results in a decrease in permeation. This could be attributed to the decreased adsorption ability of the gas molecules at higher temperatures caused by the increased velocity.<sup>53</sup> Overall, permeation of  $\text{H}_2$  and  $\text{H}_2\text{O}$  is not greatly influenced by variations of temperature in the analysed range, as the van't Hoff type temperature dependence of adsorption and the Arrhenius type temperature dependence of diffusion seem to outbalance each other. However, the  $\text{CH}_3\text{OH}$  removal shows a steep decrease in permeation between 200 °C and 250 °C. This could be induced by the critical temperature of  $\text{CH}_3\text{OH}$  at 239.9 °C, above which  $\text{CH}_3\text{OH}$  becomes a non-condensable fluid inhibiting permeation by capillary condensation.<sup>24,54</sup>

### 3.3 Membrane performance

The performance of the MR applying the base case operating parameters is illustrated in Fig. 6. The molar fractions are depicted along the length of the MR with the synthesis gas inlet shown at 0% and the counter-current sweep inlet at 100%. As expected, the molar fraction of  $\text{H}_2$  and  $\text{CO}_2$  decrease in the reaction zone along the length of the MR, while the molar fractions of  $\text{CH}_3\text{OH}$ ,  $\text{H}_2\text{O}$ , and  $\text{CO}$  increase along the reactor due to the occurring reactions. On the sweep gas side, the molar fractions of the permeating species  $\text{H}_2\text{O}$ ,  $\text{CH}_3\text{OH}$ , and  $\text{H}_2$  increase in counter-current along the length of the MR indicating the water-conducting and gas-impeding characteristics of the applied membrane. As mentioned in the modeling section,  $\text{CO}_2$  and  $\text{CO}$  are not considered to permeate through the membrane and are hence indicated on the abscissa.

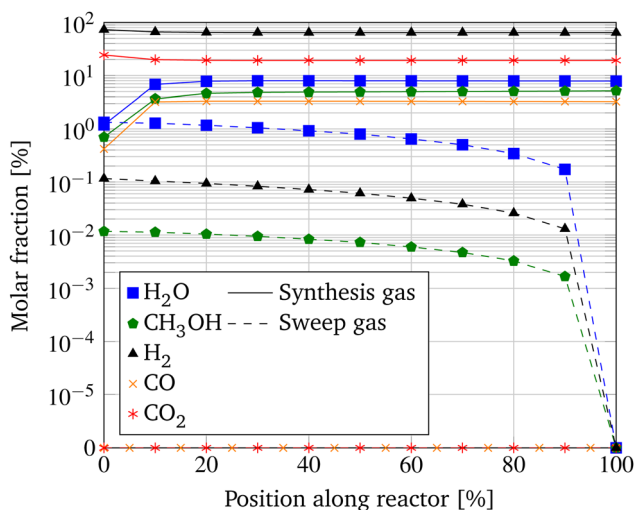


Fig. 6 Molar fractions along the length of the MR with base case parameters at a pressure of 100 bar and a temperature of 250 °C.

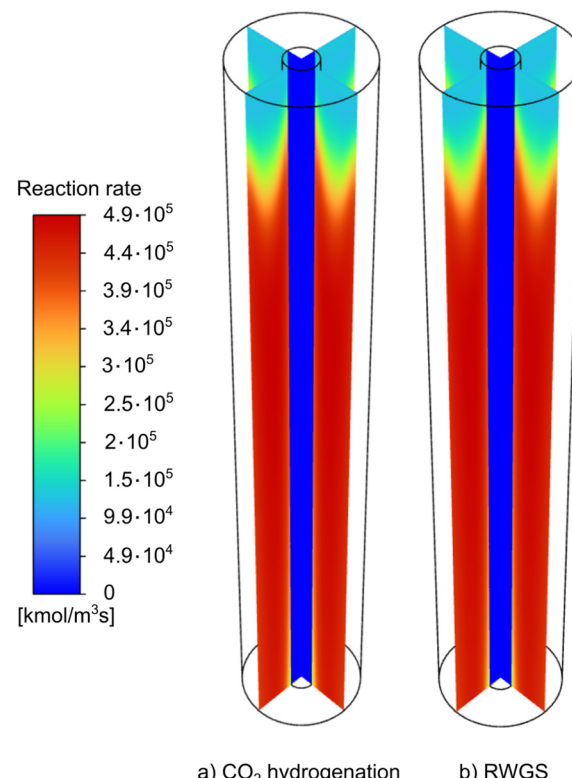


Fig. 7 Profiles of the (a)  $\text{CO}_2$  hydrogenation and (b) RWGS reaction rates along the length of the MR with base case parameters at a pressure of 100 bar and a temperature of 250 °C.

The reaction rates of the  $\text{CO}_2$  hydrogenation and the RWGS reaction as well as the temperature profile along the MR for the base case scenario are shown in Fig. 7 and 8. Conceivably, the temperature profile coincides with the distribution of the reaction rates. As shown by the colour scheme, the reaction rates first increase and remain rather constant over the length of the reactor. Due to the low heat transfer coefficient of the sweep gas, the temperature of the nitrogen stream stays fairly constant over the length of the MR.

To evaluate the performance of the MR, the  $\text{H}_2\text{O}$  removal is calculated for the base case scenario. As already indicated by the logarithmic scale of the y-axis in Fig. 6, only 7.82% of the generated  $\text{H}_2\text{O}$  is removed by the membrane. Hence, the shift of the equilibrium towards the products is small causing a negligible increase in the efficiency of the  $\text{CH}_3\text{OH}$  synthesis reaction. To validate this behavior, the simulation is repeated with impeding permeation through the membrane revealing an increase in  $\text{CO}_2$  conversion of only 0.3%.

To optimize the performance of the MR, and increase  $\text{CO}_2$  conversion and  $\text{CH}_3\text{OH}$  yield, the effects of the previously introduced parameters (GHSV, S/F,  $\text{O}_M/\text{V}_r$ ) are investigated in a full factorial design of experiment. In Table 6, the factors as well as the evaluated values are summarized.

The main effects  $E_f$  of the factors are calculated following eqn (22), with  $m$  being the number of factors and  $y_i$  the target value ( $\text{CO}_2$  conversion or  $\text{CH}_3\text{OH}$  yield) at the high-level setting



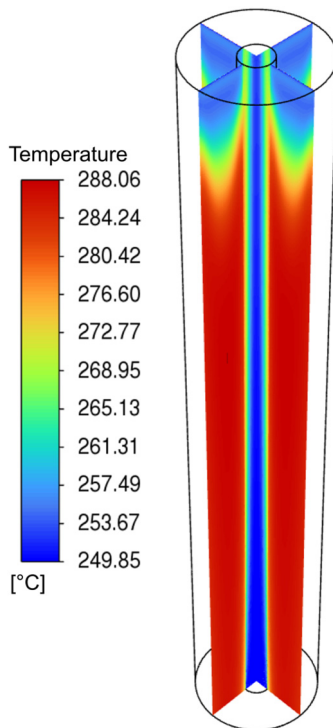


Fig. 8 Temperature profile along the length of the MR with base case parameters at a pressure of 100 bar and a temperature of 250 °C.

Table 6 Structure of the full factorial design of experiments

Number of experiment	GHSV	$\dot{V}_{\text{feed},N}$	S/F	$O_M/V_r$
	1 h <sup>-1</sup>	L min <sup>-1</sup>	—	1 m <sup>-1</sup>
1	500	0.49	1	133.33
2	5000	4.91	1	133.33
3	500	0.49	10	133.33
4	5000	4.91	10	133.33
5	500	2.45	1	26.67
6	5000	24.54	1	26.67
7	500	2.45	10	26.67
8	5000	24.54	10	26.67

of the factor ( $y_{i,+}$ ) and the low level setting of the factor ( $y_{i,-}$ ).<sup>55</sup>

$$E_f = \frac{2}{m} \cdot \sum_{i=1}^m (y_{i,+} - y_{i,-}) \quad (22)$$

In Fig. 9–11, the main effects of the parameters are depicted, showing comparable trends for CO<sub>2</sub> conversion and CH<sub>3</sub>OH yield. To identify the impact of the MR, the resulting CO<sub>2</sub> conversion and CH<sub>3</sub>OH yield of a comparable TR is added in a dashed line with round marks. For the simulation of the TR, the same CFD model is used with impeded permeation.

As shown in Fig. 9, the lower the GHSV, the higher CO<sub>2</sub> conversion and CH<sub>3</sub>OH yield. This is primarily the result of the longer residence time of the reactants in the reactor, as indicated by the increase of conversion of the TR from 29.7% to 31.3%. However, the impact of the membrane is significantly larger at a lower GHSV. While the increase in CO<sub>2</sub> conversion of

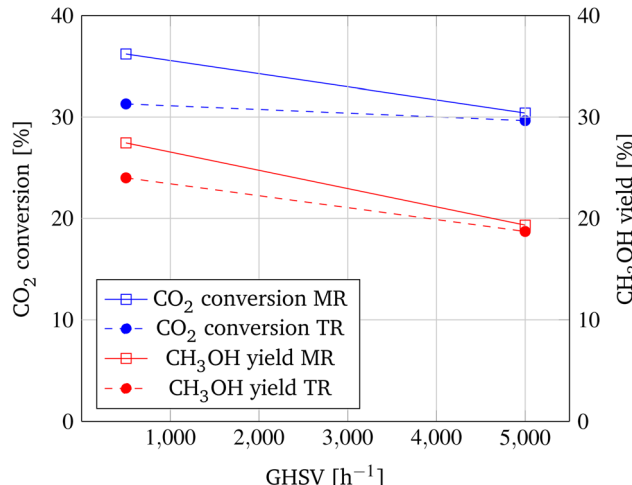


Fig. 9 Main effect of GHSV on CO<sub>2</sub> conversion and CH<sub>3</sub>OH yield at 100 bar and 250 °C.

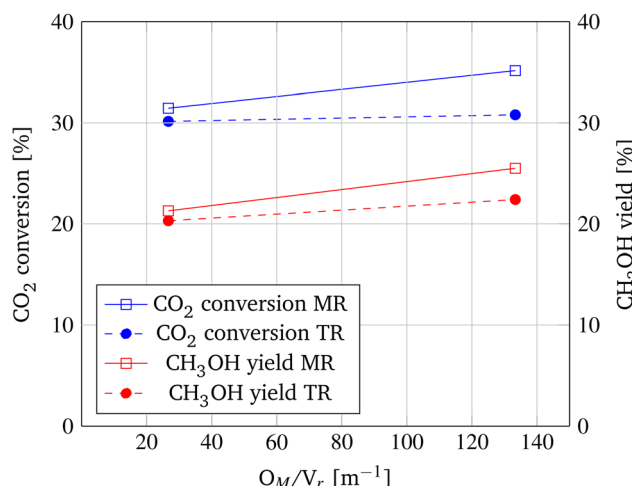


Fig. 10 Main effect of  $O_M/V_r$  ratio on CO<sub>2</sub> conversion and CH<sub>3</sub>OH yield at 100 bar and 250 °C.

the MR only accounts for an increase of 0.8% at a GHSV of 5000 h<sup>-1</sup>, at a decelerated GHSV of 500 h<sup>-1</sup> the application of the MR leads to an increase of CO<sub>2</sub> conversion of 4.9%. This is due to the increased residence time of the reaction products at the membrane and the higher adsorption ability of the gas molecules resulting from the lower velocity.<sup>24</sup> Hence, a higher amount of reaction product permeates through the membrane and is removed from the reaction zone, resulting in an enhanced shift of the chemical equilibrium and consequently an increase in CO<sub>2</sub> conversion and CH<sub>3</sub>OH yield.

Permeation seems to be the limiting factor in shifting the chemical equilibrium and enhancing conversion. As a second parameter, the ratio of membrane surface to reaction volume is investigated to accelerate permeation, enhance the shift of the chemical equilibrium, and ultimately improve CO<sub>2</sub> conversion. Therefore, while the membrane geometry is kept constant, the diameter of the reactor tube is decreased from 40 mm to

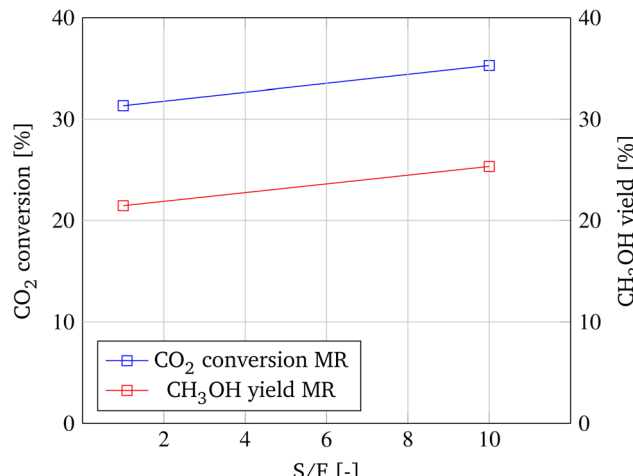


Fig. 11 Main effect of S/F ratio on CO<sub>2</sub> conversion and CH<sub>3</sub>OH yield at 100 bar and 250 °C.

20 mm, leading to a  $O_M/V_r$  ratio of  $26.7 \text{ m}^{-1}$  and  $133.3 \text{ m}^{-1}$ , respectively. As depicted in Fig. 10, at the lower  $O_M/V_r$  ratio, the performance of the MR only marginally surpasses the CO<sub>2</sub> conversion and CH<sub>3</sub>OH yield of the TR by 1.3% and 1.0%, respectively. However, when increasing the ratio of membrane surface to reaction volume, CO<sub>2</sub> conversion increases from 31.45% to 35.2% and CH<sub>3</sub>OH yield is enhanced by 4.2% compared to the TR.

Besides improving the permeation on the reaction side of the membrane, CO<sub>2</sub> conversion and CH<sub>3</sub>OH yield could be enhanced by increasing the partial pressure difference as the driving force of permeation. This can be realized by removing the permeated species inside the membrane faster from the reactor. The influence of an accelerated sweep transporting the permeated species out of the MR is shown in Fig. 11. With a ten times faster sweep, an increase of CO<sub>2</sub> conversion from 31.3% to 35.3% and an enhancement of the CH<sub>3</sub>OH yield of 3.9% is achievable.

Comparable to Fig. 6, the molar fractions of the involved species over the length of the MR with the most promising parameter compilation of a GHSV of  $500 \text{ h}^{-1}$ , a S/F ratio of 10 and a  $O_M/V_r$  ratio of  $133.3 \text{ m}^{-1}$  are displayed in Fig. 12. As before, the educts H<sub>2</sub> and CO<sub>2</sub> decrease in the reaction zone, and the permeating species H<sub>2</sub>O, H<sub>2</sub>, and CH<sub>3</sub>OH increase in counter-current in the sweep. However, in contrast to the base configuration of the MR, the molar fraction of H<sub>2</sub>O shows an increase over the first 10% of the reactor length and starts declining subsequently, indicating the functionality of the membrane reactor. As a result, the chemical equilibrium of the hydrogenation reaction is shifted, and the molar fraction of CH<sub>3</sub>OH increases over the entire length of the reactor rather than remaining nearly constant after an initial steep increase when comparing it to the base case configuration in Fig. 6. Due to the optimization of the constructive and operational configuration of the MR, the H<sub>2</sub>O removal is increased to 88.1%. To identify the impact of the MR, the simulation is repeated with impeding permeation through the membrane, disclosing an increase in CO<sub>2</sub> conversion by the membrane of 14.0%.

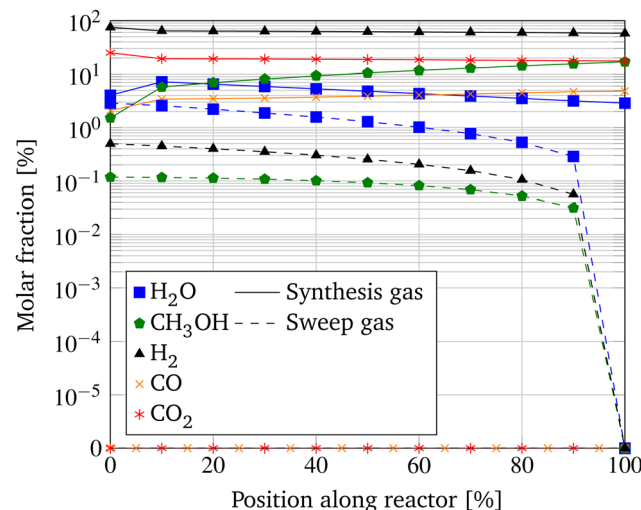


Fig. 12 Molar fractions along the length of the MR with best case parameters (GHSV =  $500 \text{ h}^{-1}$ , S/F ratio = 10,  $O_M/V_r$  ratio =  $133.3 \text{ m}^{-1}$ ) at a pressure of 100 bar and a temperature of 250 °C.

Finally, a fourth influential factor, a potential pressure difference between reaction zone and membrane is investigated for the previously introduced most promising parameter compilation (GHSV =  $500 \text{ h}^{-1}$ ,  $\dot{V}_{\text{feed},N} = 0.49 \text{ L min}^{-1}$ , S/F-ratio = 10,  $O_M/V_r$ -ratio =  $26.67 \text{ m}^{-1}$ ). Based on the manufacturer's statements, the membrane is capable of withstanding a pressure difference of up to 100 bar. Hence, a 99 bar pressure difference is adjusted for the simulation. The results are depicted in Fig. 13, showing an increase of CO<sub>2</sub> conversion of 6.1% and an enhancement of CH<sub>3</sub>OH yield of 4.3% when the pressure difference is applied.

This increase is caused by the greater partial pressure difference, the driving force of permeation, that is depended on the prevalent absolute pressure. In the dashed lines, the comparable outcomes of the TR are depicted, illustrating the maximum increase of CO<sub>2</sub> conversion of 20.1% and the maximum increase of CH<sub>3</sub>OH yield of 14.8% when using the MR.

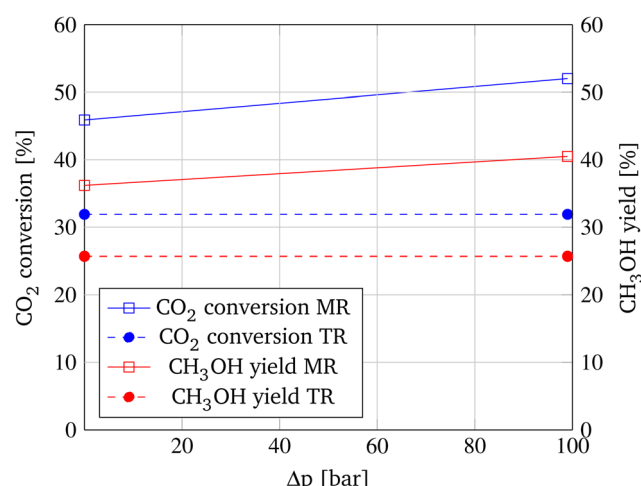


Fig. 13 Impact of  $\Delta p$  across the membrane on CO<sub>2</sub> conversion and CH<sub>3</sub>OH yield at 100 bar and 250 °C.



In the most optimal configuration ( $\text{GHSV} = 500 \text{ h}^{-1}$ ,  $\dot{V}_{\text{feed},N} = 0.49 \text{ L min}^{-1}$ ,  $\text{S/F-ratio} = 10$ ,  $\text{O}_M/V_r\text{-ratio} = 26.67 \text{ m}^{-1}$ ,  $\Delta p = 99 \text{ bar}$ ), the application of the MR results in a maximum  $\text{CO}_2$  conversion of 52.0% exceeding the equilibrium conversion at a pressure of 100 bar and a temperature of 250 °C by 11.7%.<sup>9</sup> The methanol yield is increased to a maximum of 40.5%, transcending the equilibrium yield by 5.2%.<sup>9</sup> These roughly 20% increases compared to the TR result in the reduction of the necessary recycling volume flow and the corresponding energy consumption for the recycling compression by about 1/5. When assessing the added value of a membrane reactor for methanol synthesis, a surpassing of 10%  $\text{CO}_2$  conversion illustrates the great potential of membrane reactors for equilibrium-limited reactions.

### 3.4 Findings of the full-factorial design of experiments

The findings of this study show the importance of optimization for the construction as well as the operation when implementing MRs instead of TRs. It shows, that for a comparison of MR and TR in any application, it is not sufficient to just apply the optimal parameters of a TR to the substituting MR. As a guideline for the optimization of MRs, in general, following key parameters should be regarded:

- Ratio between reaction and permeation

Permeation seems to be the rate determining step to shift the equilibrium towards the products. Hence, when the residence time of the permeating species is too low or the diffusion towards the membrane takes too long, too little permeating species are removed from the reaction zone and the membrane has negligible impact. Two parameters are determined influencing the ratio between reaction and permeation:

- (1)  $\text{GHSV}$ : when decreasing the  $\text{GHSV}$ , the feed volume flow is decreased. Thus, the residence time of the reactants is increased leading to an enhanced permeation and a shift in the chemical equilibrium of the synthesis.
- (2)  $\text{O}_M/V_r$ : when increasing the ratio between surface area of the membrane and volume of the reaction zone, a shorter distance needs to be surpassed by the permeating species towards the membrane. Thus, more reaction products are removed from the reaction zone shifting the equilibrium towards higher conversion.

- Partial pressure difference

Since the partial pressure difference between the reaction zone and sweep side is the driving force for permeation, an increase in partial pressure difference results in a higher conversion. Two parameters are identified to influence the partial pressure difference:

- (1) Total pressure difference: when depressurizing the sweep stream, a difference in the total pressure increases the partial pressure difference leading to a significant shift in the equilibrium.
- (2) Sweep velocity: on the inside of the membrane, a sweep stream removes the permeated species from the reactor. The faster this transportation occurs, the larger the partial pressure difference and the greater the increase in conversion.

## Conclusions

This work determines key constructive and operating parameters for a membrane reactor for methanol synthesis *via*  $\text{CO}_2$  hydrogenation. As the reaction of  $\text{CO}_2$  and  $\text{H}_2$  to  $\text{CH}_3\text{OH}$  is thermodynamically limited by the chemical equilibrium, the achievable conversion is restricted. To overcome the chemical equilibrium, membrane reactors are adopted, removing reaction products from the reaction zone and, consequently, enhancing conversion. Eventually, the required expensive recirculation of unconverted reactants can be downsized, resulting in a more efficient methanol production approach. For the parameter study, a sophisticated CFD model of the MR with a NaA zeolite membrane is developed, incorporating the kinetics of the chemical reactions as well as the permeation of diffusing species. Unlike previous simulative studies on membrane reactors for methanol synthesis, in this work, permeation is described in more detail by the M-S approach that does not disregard interactions between competing permeating species. Moreover, the distinct characteristics of pervaporating water-alcohol mixtures in zeolite membranes are considered.

After first investigating the correlation between operation conditions and  $\text{CO}_2$  conversion and  $\text{CH}_3\text{OH}$  yield, revealing the optimal operating conditions for methanol synthesis in a MR at a temperature of 250 °C and pressure of 100 bar, the permeation through the membrane is characterized. Therefore, the parameter of the species removal, depicting the effect of the membrane on the permeating species, is introduced, revealing the temperature independence of the permeation of  $\text{CH}_3\text{OH}$  and  $\text{H}_2$ . On the contrary, the characterization shows the significant decrease in methanol permeation past the critical temperature due to the inhibition of permeation by capillary condensation. After analyzing the membrane performance in a base case scenario, a full-factorial design of experiment is conducted to optimize operational and construction parameters. The findings show that the impact of the MR is higher for lower  $\text{GHSVs}$ , a higher ratio of membrane surface to catalyst volume, higher sweep volume flows, and higher total pressure differences across the membrane. These parameters can be summarized in two general categories that have to be optimized for membrane reactors for industrial applications: the ratio between reaction and permeation and the permeation driving force. In the most optimal configuration, the application of the MR results in an increase of  $\text{CO}_2$  conversion of 20.6% and a 16.0% enhanced  $\text{CH}_3\text{OH}$  yield. With the surpassing of the chemical equilibrium, this study shows the potential to shift the chemical equilibrium of methanol synthesis in membrane reactors towards the products, reducing recycling flows and necessary compression energy.

Based on the findings of this study, several research questions can be proposed: considering the significant impact of the pressure difference across the membrane, experimental high pressure investigations of the MR should be conducted to analyze the durability of the membrane and help identify the actual influence the pressure difference can have on  $\text{CO}_2$  conversion and  $\text{CH}_3\text{OH}$  yield. Moreover, long-term experimental



investigations of the MR could provide insights into the lifetime of the membrane, which is crucial for the feasibility of industrial applications. Furthermore, these long-term tests could reveal degradation effects of the membrane in the process that are neither known nor considered in literature. The experimental results can finally help to evaluate the impact MRs for methanol synthesis can have on an industrial scale.

Recapitulating, the results of the study on construction parameters and operating guidelines show how crucial optimization of the reactor design and operating conditions are especially important for membrane reactors and can help to increase the understanding of the possible impact membrane reactors can have on methanol synthesis but also on various other applications where the use of membrane reactors is discussed.

## Author contributions

Theresa Hauth: conceptualization, methodology, formal analysis, investigation, writing – original draft; Konstantin Pielmaier: software, investigation, visualization, writing – original draft; Vincent Dieterich: conceptualization, methodology, investigation, writing – review & editing; Nicolas Wein: software, investigation, writing – review & editing; Hartmut Spliethoff: conceptualization, writing – review & editing, supervision, funding acquisition; Sebastian Fendt: conceptualization, writing – review & editing, supervision, project administration, funding acquisition.

## Data availability

The data supporting this article have been included as part of the ESI.†

## Conflicts of interest

There are no conflicts to declare.

## Acknowledgements

This study was carried out in the framework of the project H2-Reallabor Burghausen – ChemDelta Bavaria (project no.: 03SF0705B) and sponsored by the Federal Ministry of Education and Research (Germany). The financial support is gratefully acknowledged. In addition, the authors acknowledge the cooperation within the Network TUM.Hydrogen and PtX.

## Notes and references

1. H. Lee and J. Romero, *IPCC, 2023: Climate Change 2023: Synthesis Report. Contribution of Working Groups I, II and III to the Sixth Assessment Report of the Intergovernmental Panel on Climate Change.*, Intergovernmental Panel on Climate Change (IPCC), 2023.

2. U. EPA, *Overview of Greenhouse Gases*, 2015, Accessed: 2024-04-12.
3. M. Bui, C. S. Adjiman, A. Bardow, E. J. Anthony, A. Boston, S. Brown, P. S. Fennell, S. Fuss, A. Galindo, L. A. Hackett, J. P. Hallett, H. J. Herzog, G. Jackson, J. Kemper, S. Krevor, G. C. Maitland, M. Matuszewski, I. S. Metcalfe, C. Petit, G. Puxty, J. Reimer, D. M. Reiner, E. S. Rubin, S. A. Scott, N. Shah, B. Smit, J. P. M. Trusler, P. Webley, J. Wilcox and N. Mac Dowell, *Energy Environ. Sci.*, 2018, **11**, 1062–1176.
4. S. Kanuri, S. Roy, C. Chakraborty, S. P. Datta, S. A. Singh and S. Dinda, *Int. J. Energy Res.*, 2021, **46**, 5503–5522.
5. A. Tremel, P. Wasserscheid, M. Baldauf and T. Hammer, *Int. J. Hydrogen Energy*, 2015, **40**, 11457–11464.
6. P. Research, *Market size of methanol worldwide in 2021, with a forecast until 2030 (in billion U.S. dollars)*, 2022, Accessed: 2024-07-18.
7. M. M. S. A. (MMSA), *MMSA Global Methanol Supply and Demand Balance*, 2023, Accessed: 2024-04-12.
8. S. Navarro-Jaén, M. Virginie, J. Bonin, M. Robert, R. Wojcieszak and A. Y. Khodakov, *Nat. Rev. Chem.*, 2021, **5**, 564–579.
9. V. Dieterich, A. Buttler, A. Hanel, H. Spliethoff and S. Fendt, *Energy Environ. Sci.*, 2020, **13**, 3207–3252.
10. X. Jiang, X. Nie, X. Guo, C. Song and J. G. Chen, *Chem. Rev.*, 2020, **120**, 7984–8034.
11. G. Bozzano and F. Manenti, *Prog. Energy Combust. Sci.*, 2016, **56**, 71–105.
12. S. Mbatha, R. C. Everson, N. M. Musyoka, H. W. Langmi, A. Lanzini and W. Brilman, *Sustainable Energy Fuels*, 2021, **5**, 3490–3569.
13. M. Ebrahimzadeh Sarvestani, O. Norouzi, F. Di Maria and A. Dutta, *Energy Convers. Manage.*, 2024, **302**, 118070.
14. Q. I. Roode-Gutzmer, D. Kaiser and M. Bertau, *ChemBioEng Rev.*, 2019, **6**, 209–236.
15. R. Raso, M. Tovar, J. Lasobras, J. Herguido, I. Kumakiri, S. Araki and M. Menéndez, *Catal. Today*, 2021, **364**, 270–275.
16. M. Bos and D. Brilman, *Chem. Eng. J.*, 2015, **278**, 527–532.
17. M. J. Bos, Y. Slotboom, S. R. A. Kersten and D. W. F. Brilman, *Ind. Eng. Chem. Res.*, 2019, **58**, 13987–13999.
18. M. Kuczynski, M. Oyevar, R. Pieters and K. Westerterp, *Chem. Eng. Sci.*, 1987, **42**, 1887–1898.
19. A. Arora, S. S. Iyer, I. Bajaj and M. M. F. Hasan, *Ind. Eng. Chem. Res.*, 2018, **57**, 14143–14161.
20. V. Dieterich, N. Wein, H. Spliethoff and S. Fendt, *Adv. Sustainable Syst.*, 2022, **6**, 1–12.
21. K. Atsonios, K. D. Panopoulos and E. Kakaras, *Int. J. Hydrogen Energy*, 2016, **41**, 792–806.
22. R. Struis, S. Stucki and M. Wiedorn, *J. Membr. Sci.*, 1996, **113**, 93–100.
23. H. Homa and B. Torsten, *ACS Sustainable Chem. Eng.*, 2021, **9**, 7620–7629.
24. F. Gallucci, L. Paturzo and A. Basile, *Chem. Eng. Process.*, 2004, **43**, 1029–1036.
25. T. V. Tran, N. Le-Phuc, T. H. Nguyen, T. T. Dang, P. T. Ngo and D. A. Nguyen, *Int. J. Chem. React. Eng.*, 2017, **16**, 1–14.
26. H. Li, C. Qiu, S. Ren, Q. Dong, S. Zhang, F. Zhou, X. Liang, J. Wang, S. Li and M. Yu, *Science*, 2020, **367**, 667–671.



27 W. Yue, Y. Li, W. Wei, J. Jiang, J. Caro and A. Huang, *Angew. Chem., Int. Ed.*, 2021, **60**, 18289–18294.

28 M. Seshimo, B. Liu, H. R. Lee, K. Yogo, Y. Yamaguchi, N. Shigaki, Y. Mogi, H. Kita and S.-I. Nakao, *Membranes*, 2021, **11**, 505.

29 F. Samimi, N. Hamedi and M. R. Rahimpour, *J. Environ. Chem. Eng.*, 2019, **7**, 102813.

30 G. Barbieri, G. Marigliano, G. Golemme and E. Drioli, *Chem. Eng. J.*, 2002, **85**, 53–59.

31 K. Ountaksinkul, P. Vas-Umnuay, N. Kasempremchit, P. Bumroongsakulswat, P. Kim-Lohsoontorn, T. Jiwanuruk and S. Assabumrungrat, *Chem. Eng. Process.*, 2019, **136**, 191–200.

32 H. Hamedi, T. Brinkmann and S. Shishatskiy, *Membranes*, 2021, **11**, 596.

33 H. Huang, R. Can Samsun, R. Peters and D. Stolten, *Chem. Eng. Sci.*, 2022, **252**, 117284.

34 J. A. Wesselingh and R. Krishna, *Mass transfer in multi-component mixtures*, VSSD, 2006.

35 R. Krishna and J. M. van Baten, *Langmuir*, 2010, **26**, 10854–10867.

36 R. Krishna and R. Baur, *Chem. Eng. J.*, 2004, **97**, 37–45.

37 R. Krishna and J. M. van Baten, *J. Membr. Sci.*, 2010, **360**, 476–482.

38 G. Graaf, E. Stamhuis and A. Beenackers, *Chem. Eng. Sci.*, 1988, **43**, 3185–3195.

39 G. Graaf, H. Scholtens, E. Stamhuis and A. Beenackers, *Chem. Eng. Sci.*, 1990, **45**, 773–783.

40 K. Bussche and G. Froment, *J. Catal.*, 1996, **161**, 1–10.

41 D. Mignard and C. Pritchard, *Chem. Eng. Res. Des.*, 2008, **86**, 473–487.

42 F. Nestler, V. P. Müller, M. Ouda, M. J. Hadrich, A. Schaad, S. Bajohr and T. Kolb, *React. Chem. Eng.*, 2021, **6**, 1092–1107.

43 G. Graaf, P. Sijtsema, E. Stamhuis and G. Joosten, *Chem. Eng. Sci.*, 1986, **41**, 2883–2890.

44 S. Guo, C. Yu, X. Gu, W. Jin, J. Zhong and C.-L. Chen, *J. Membr. Sci.*, 2011, **376**, 40–49.

45 K. O. Murdmaa and V. V. Serpinskii, *Bull. Acad. Sci. USSR, Div. Chem. Sci.*, 1972, **21**, 417–420.

46 T. C. Bowen, R. D. Noble and J. L. Falconer, *J. Membr. Sci.*, 2004, **245**, 1–33.

47 P. Ciavarella, H. Moueddeb, S. Miachon, K. Fiaty and J.-A. Dalmon, *Catal. Today*, 2000, **56**, 253–264.

48 S. Beyaz Kayiran and F. Lamari Darkrim, *Surf. Interface Anal.*, 2002, **34**, 100–104.

49 M. Pera-Titus, C. Fit  , V. Sebasti  n, E. Lorente, J. Llorens and F. Cunill, *Ind. Eng. Chem. Res.*, 2008, **47**, 3213–3224.

50 R. Krishna and J. Wesselingh, *Chem. Eng. Sci.*, 1997, **52**, 861–911.

51 R. Krishna, *NATO Science Series II: Mathematics Physics and Chemistry*, Kluwer Academic Publishers, 2006, pp. 211–240.

52 R. Krishna and J. M. van Baten, *J. Membr. Sci.*, 2013, **430**, 113–128.

53 G. Song, W. Zhou, C. Li, Z. Wang, F. Hu, T. Wang, Z. Li, A. Tang, M. P. Harold, S. Liu and S. Kawi, *J. Membr. Sci.*, 2023, **678**, 121666.

54 P. Linstrom, *NIST Chemistry WebBook, NIST Standard Reference Database 69*, National Institute of Standards and Technology, 1997.

55 J. Antony, *A Systematic Methodology for Design of Experiments*, Elsevier, 2014, pp. 33–50.

